CHAPTER 7

EFFECT OF SURFACE MODIFICATION ON PRE-HOT CORROSION-EROSION BEHAVIOUR OF TYPE 446 STAINLESS STEEL

7.1 INTRODUCTION

The present work extends our previous study on the effect of pre-hot-corrosion on erosion behavior of Type 446SS at 550, 650 and 750℃. Here, USSP treatment is an added factor to see its effect on hot corrosion resistance of this steel. Several processes of surface modifications and microstructure development, like, severe plastic deformation, surface coatings, ball milling, shot peening, LSP and USSP have been employed to intensify the surface properties of the structural component [136,187,188]. With the objective of improving the materials resistance to corrosion when exposed to the corrosive environment, the ultrasonic shot peening (USSP) process is adapted as a surface modification technique to impart compressive stress to the surface. USSP is a relatively new technique of grain refinement that significantly improves the mechanical properties of metallic materials by creating compressive residual stress through ball impact on the material surface and brings no change to their chemical composition [138,189]. These impacting balls act as a hammer creating indentation or semi-sphere, thereby increasing the hardness of the surface. This cumulative effect of grain refinement and compressive residual stresses in the surface and sub-surface regions can increase corrosion resistance and thus, the life span of the component [143,190]. Under the effect of USSP treatment, the faster diffusion of chromium ions along grain boundaries as

compared to through grain themselves improves the corrosion and oxidation properties of ferritic steel [144].

USSP generates grain refinement along with other defects that provide a short-circuit path for the diffusion of beneficial solute atoms at the free surface and creates a protective oxide layer [140]. In general, plastic deformation techniques have proved to be instrumental in improving the corrosion resistance of the metallic material, yet, an adverse theory also prevails alongside. The corrosion rate increases two folds in the presence of erosion, which is responsible for generating flakes on the surface under the repeated impact of particles [191]. The effect of USSP on hot corrosion-erosion behavior of high chromium ferritic steel is hardly investigated and reported. This investigation highlights the dissemination of chromium to the surface forming a layer of chromium oxide, which is responsible to inhibit the outward diffusion of iron and reduce the iron-based scales formation.

7.2 RESULTS

7.2.1 Characterization of USSP treated surface

Surface roughness of USSP treated surface

The optical micrograph of the USSPed samples clearly shows (Fig. 7.1) that the effect of shot peening leads to grain refinement to a depth of ~300 µm. This finding is further substantiated by the microhardness profile where the average hardness is recorded as 315 ± 8 HV on the 2min shot-peened surface and varies significantly to a depth of ~250 µm (Fig.7.2). The average roughness (R_a) illustrates that the R_a value for the non-USSPed surface is lesser than the USSPed surface. This aspect of roughness is manifested in surface topography of the sample where dimples are apparently seen on the surface. Further, with subsequent increase in impact duration, the dimples are seen to be deeper,

and crest cracks are formed which are the cause of chipping and flake/scale formation (Fig.7.3 (a-c)). Also, the surface experiences a progressive increase in R_a from 2.36 to 3.25µm (Fig.7.4).

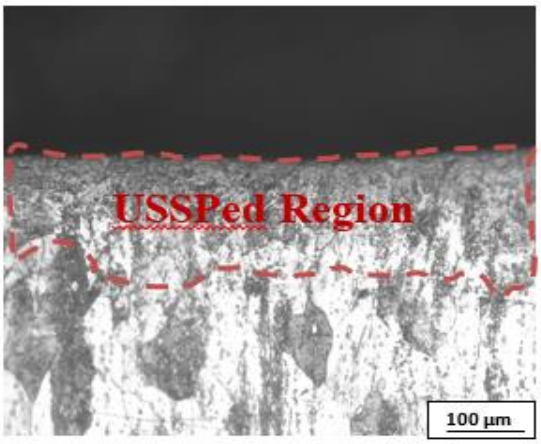

Fig. 7.1: Cross-sectional optical micrograph of 2 min USSPed sample.

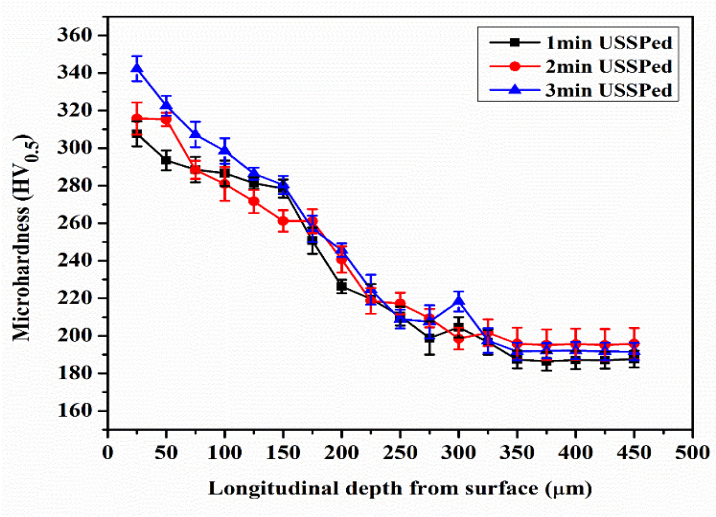

Fig. 7.2: Micro-hardness variation along the depth from the surface.

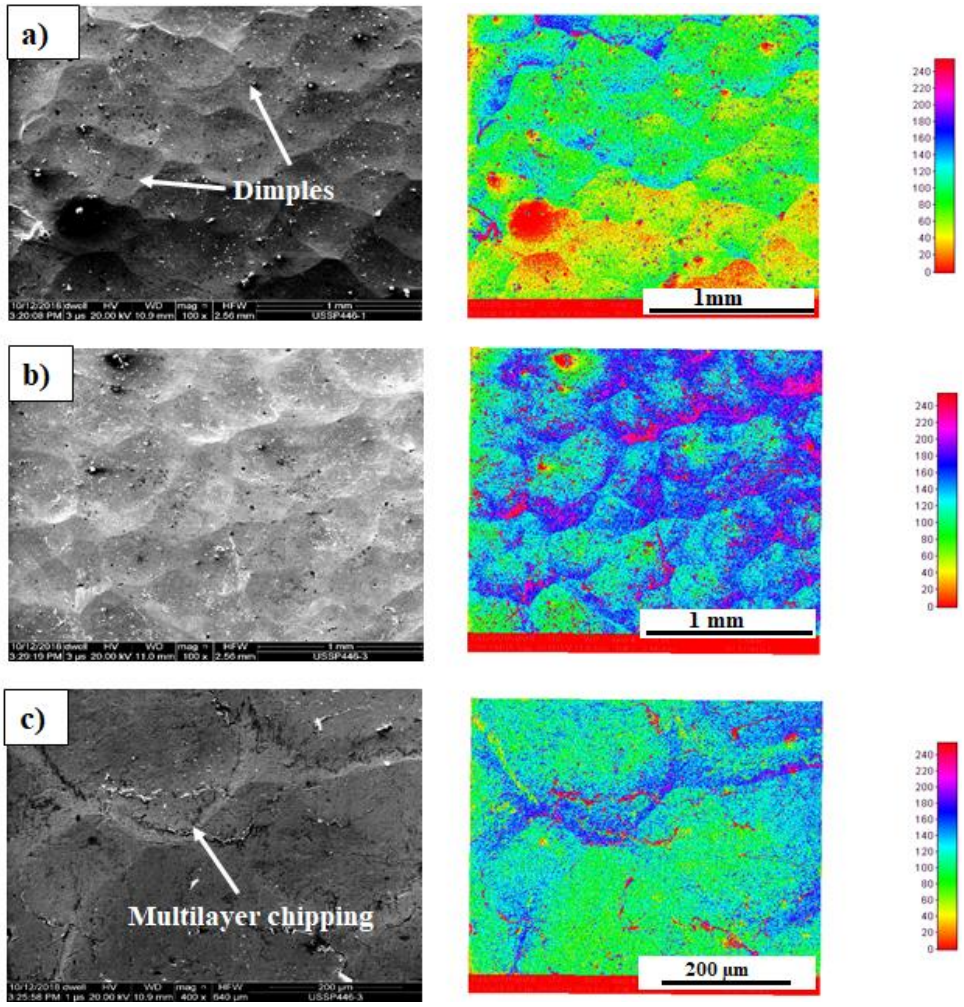

Fig. 7.3: Surface topography image of Type 446SS samples **(a)** 1min USSPed, **(b)** 2 min USSPed, and **(c)** 3 min USSPed.

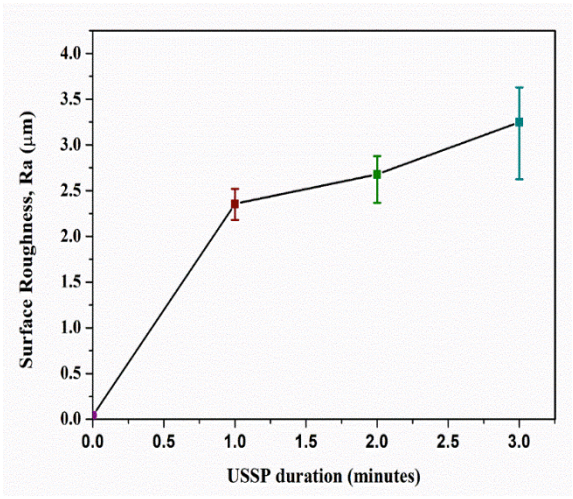

Fig. 7.4: Average roughness variation with USSP duration.

Characterization of USSPed layer

X-ray diffraction of as-received material exclusively shows the peaks of iron (Fig. 7.5). These patterns are seen to undergo peak broadening and shifting when subjected to USSP, which is evident in the enlarged view of (211). This behaviour is attributed to surface nano-crystallized (SNC) layer formation where the grain refinement leads to peak broadening, and the peak shifting is an outcome of lattice strain. Scherrer and Wilson equation [192] and Williamson Hall equation [193] were employed to calculate the average crystallite size and micro-strain respectively. Taking into account the three Bragg reflection peaks, the average crystallite size was calculated using the following equation:

$$t = \frac{0.9\lambda}{B\cos\theta} \tag{7.1}$$

The following equation was used to calculate micro-strain,

$$B\cos\theta = [\frac{0.9\lambda}{t}] + [4\varepsilon\sin\theta] \tag{7.2}$$

In the above equations,

λ = X-ray wavelength

t = effective crystallite size

θ = Bragg angle and

B = line broadening

ε = micro-strain (root mean square)

The results are presented in Table 7.1. As seen in Fig.7.6, the average crystallite size decreased from 65 nm to 52 nm and there was a considerable increase in micro-strain with the increase in USSP duration.

Table 7.1: Average crystallite size in SNC region of USSPed specimen.

USSP duration (sec)	Average crystallite size (nm)	Mean Lattice Strain (%)
60	65.7	0.179
120	64.8	0.208
180	52.1	0.225

Bright-field TEM micrograph of the as-received sample shows primary phase ferrite with some retained austenite. Also, some carbides precipitates are seen (Fig. 7.7 (a, b)). The bright-field TEM micrograph of the USSPed sample shows a high density of dislocation labyrinth within the grain and is seen to increase with the increase in USSP duration. The ring-type pattern in selected area diffraction (SAD) acknowledges the refinement of original coarse grain to nanograins (Fig. 7.7 (c,d)).

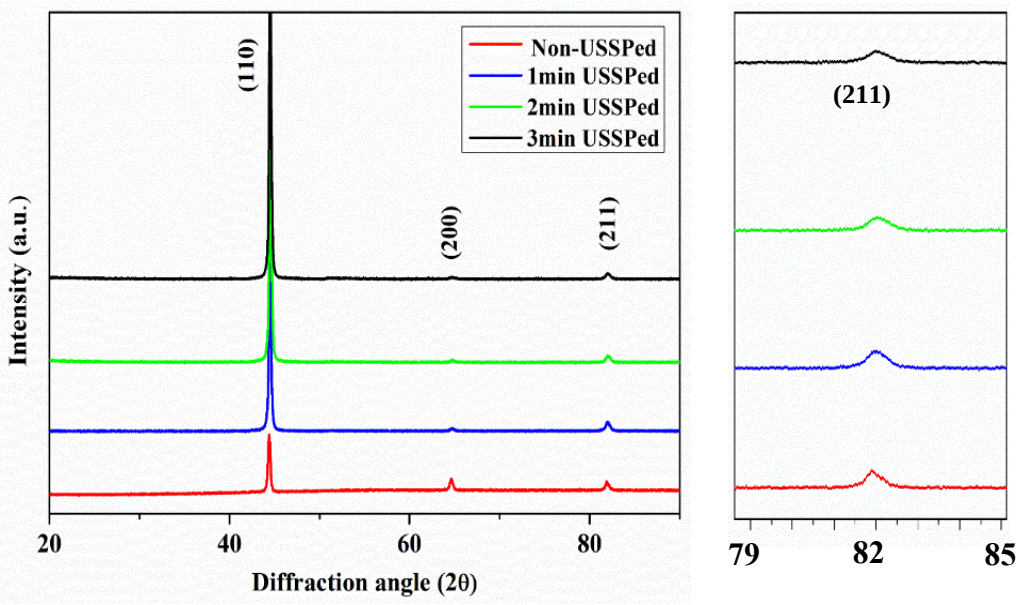

Fig. 7.5: X-ray diffraction of the non-USSPed specimen and variable time USSPed samples.

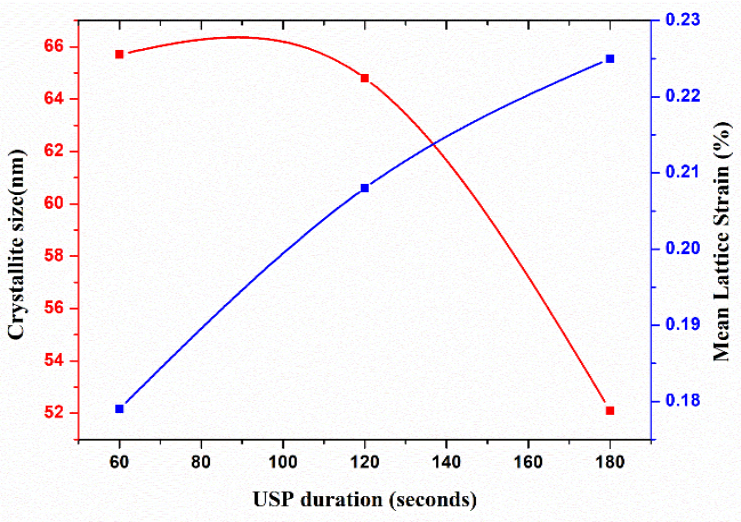

Fig. 7.6: Average crystallite size and Mean lattice strain variation with USSP duration.

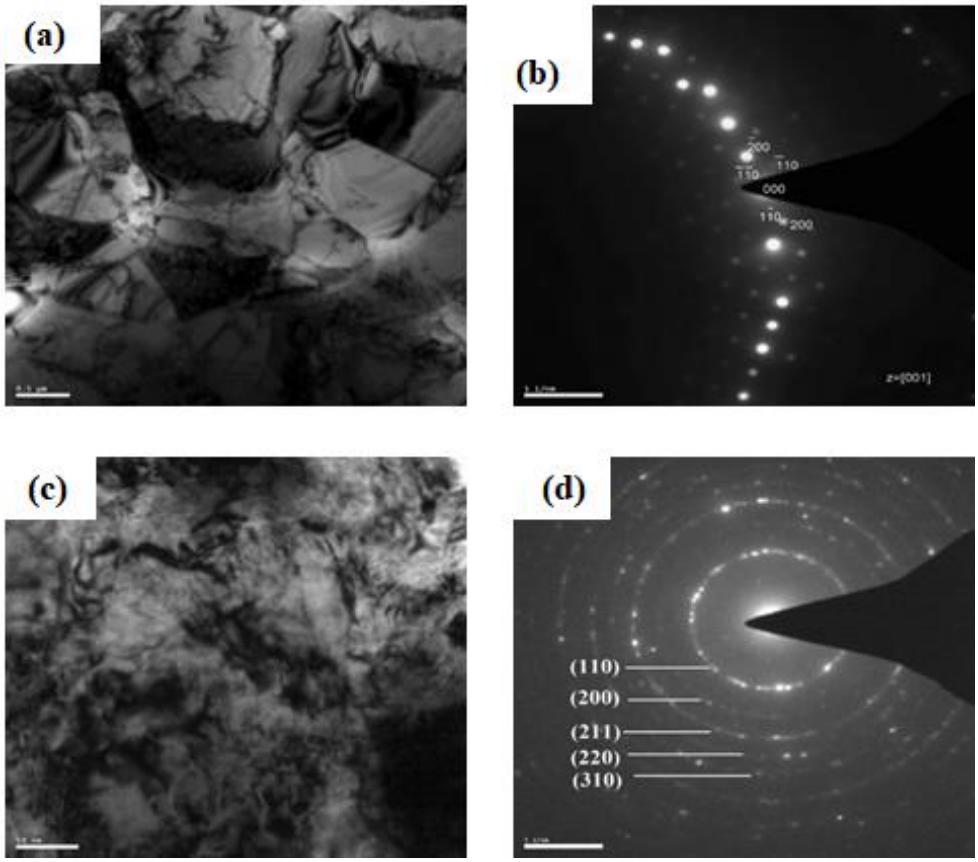

Fig. 7.7: TEM micrographs of Type 446SS **(a, b)** Non-USSPed, and **(c, d)** 2min USSPed.

7.2.2 Characterization of hot-corrosion

Macrographs of USSPed samples and Weight gain under hot Corrosion

USSPed surface coated with the salt mixture when exposed to 550℃ is almost free from any reaction on the surface and, therefore, insignificant weight gain is recorded. Consecutively, exposing the samples to a higher temperature at 650 and 750℃, a substantial increase in weight is visible, as shown in the curve (Fig. 7.8). Comparing these samples to the non-USSPed surface, under the same conditions of hot-corrosion, it is observed that the weight gain per unit area at 550, 650 and 750℃ diminished by 55, 41.71 and 27.64 % respectively, for 2min of USSP treated surface. This is due to the increase in fluidity with the rise in temperature and, therefore, the corrosion resistance of the USSP sample decreases.

Figure 7.9 shows the macrograph of the corroded surface featured using a digital camera. The surface exposed to 550℃ have a salt layer deposited in the dimples created due to shot peening, and the oxide layer is formed on the upper crest of the surface. Thus, the appearance of the sample is olive green with an oxide fraction appearing grey in colour (Fig. 7.9 a). But, at 650℃, the appearance changes to dark with heavy flaking and spalling of the scale (Fig. 7.9 b). Similarly, when exposed to 750℃, the chances of oxide formation are reduced under this high-temperature corrosion effects and surface appearance becomes pale violet in colour (Fig. 7.9 c) with debris like spallation.

Diffusion of corrosive species and surface morphology of corroded surface

The diffusion of the corrosive species is never homogeneous and, therefore, the scales formed during corrosive species attack is non-uniform. Thus, the average feature of the surface is recorded with the help of SEM. The aggressive environment responsible for the degradation of the surface shows slender behaviour at 550℃ as evident from the

rod-like structure (Fig. 7.10 a), whereas at 650℃ iron and chromium oxide scales (Fig. 7.10 b) having Allium flowers like structures are seen. Formation of a dense blister-like orbicular structure at 750℃ is indicative of mainly iron and chromium oxides (Fig. 7.10 c), as confirmed by EDS analysis of the top surface.

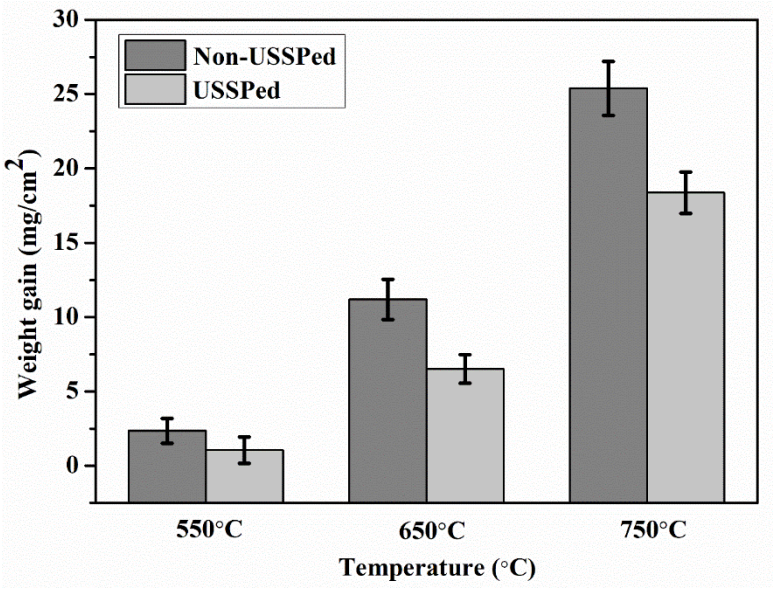

Fig. 7.8: Weight gain per unit area vs Temperature during hot corrosion of Non-USSPed and 2min USSPed samples at 550, 650 and 750℃ for 20 h in air.

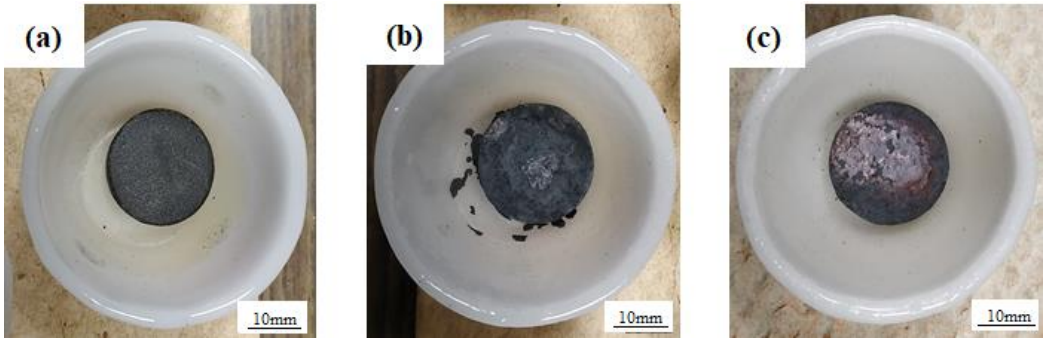

Fig. 7.9: Macrograph of 2min USSPed and hot corroded samples for 20 h at: **(a)** 550℃ **(b)** 650℃, and **(c)** 750℃.

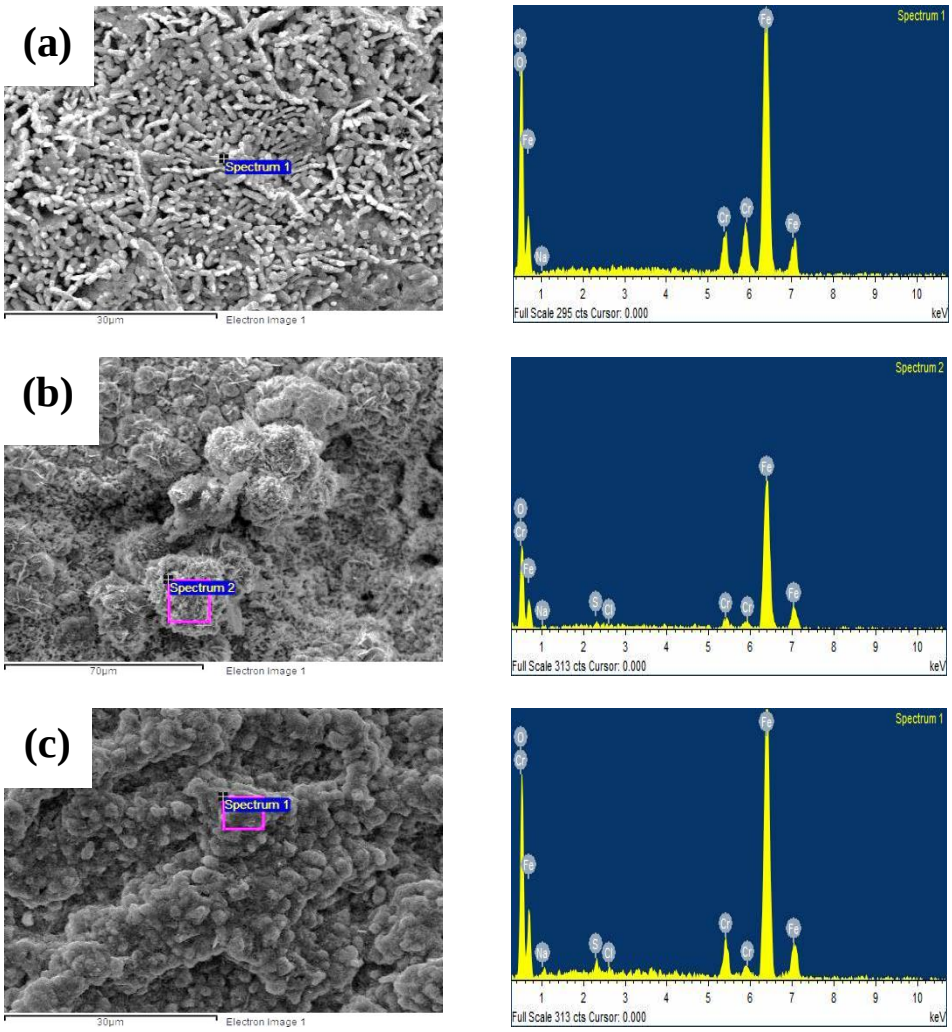

Fig. 7.10: SEM/EDX showing morphology and concentration of different elements of salt mixture deposited 2min USSPed sample exposed at **(a)** 550℃ **(b)** 650℃, and **(c)** 750℃ for 20 h.

XRD analysis and Cross-sectional elemental mapping of hot-corroded samples

The process of corrosion is largely dominated by the products formed during hot-corrosion in the initial stage. The XRD pattern for shot-peened uncoated and shot-peened two salt mixture coated samples exposed to high-temperature corrosion at 550, 650 and 750℃ (Fig. 7.11) shows the formation of oxides and sulfides like Cr_2O_3, $FeCr_2O_4$, Fe_2O_3, and FeS_2, which are deleterious to the surface of the material. The hot corrosion test at 550, 650 and 750℃, for 20 h revealed the invasion of corrosion products on the surface. The depth of invasion was characterized by sectioning the sample longitudinally from

the center. Severe corrosion is achieved at 750℃ where a thick delaminated layer of ~ 27µm is seen with few fissure cracks and several pits (Fig. 7.12a). These cracks render the materials surface weak to resist any mechanical impacts and, offer the least resistance to erosion. The effect of the salt coating is seen to be negligible at 550℃, as no significant traces of corrosion products are detected due to eutectic melting of the salt mixture being 628℃. Depth of penetration in case of 650℃ is nearly the same as 750℃ hot corrosion test, with a passive layer thickness of ~19µm and narrow cracks and slits formed on the surface (Fig. 7.12b). When examined using secondary electron (SE) x-ray mappings, the depleted concentration of chromium and the increased concentration of iron and oxygen strengthen the findings of eutectic compounds formation [179]. It is evident that oxide scale formation is thick and dense at 750℃ (Fig 7.13) and thin and subtle at 650℃ (Fig.7.14).

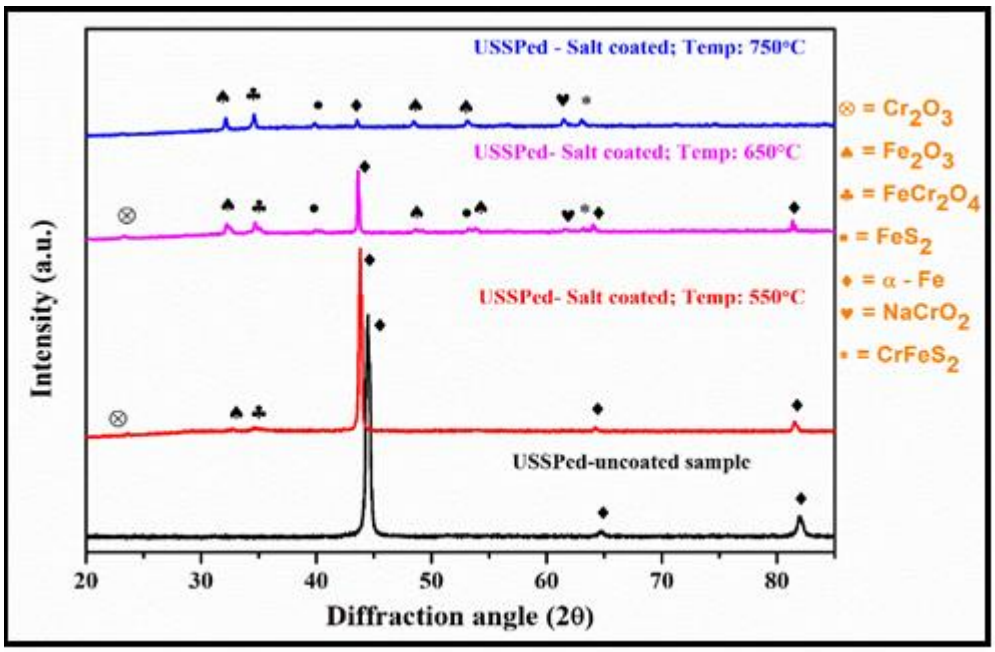

Fig. 7.11: XRD pattern of the oxides formed during hot corrosion of salt mixture coated 2 min USSPed samples for 20 h under variable temperature.

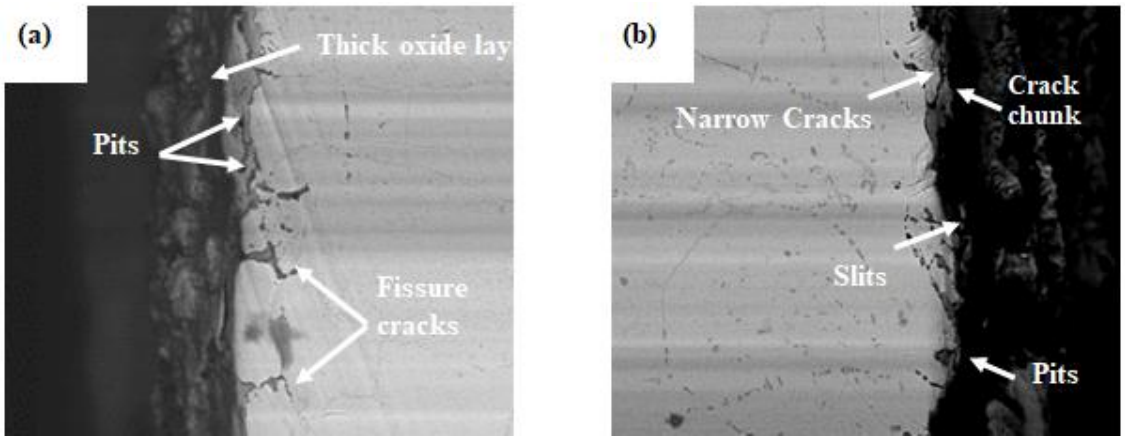

Fig. 7.12: Cross-sectional SEM micrograph of hot corroded 2min USSPed samples showing the effect of corrosive species diffusion at **(a)** 750℃, and **(b)** 650℃.

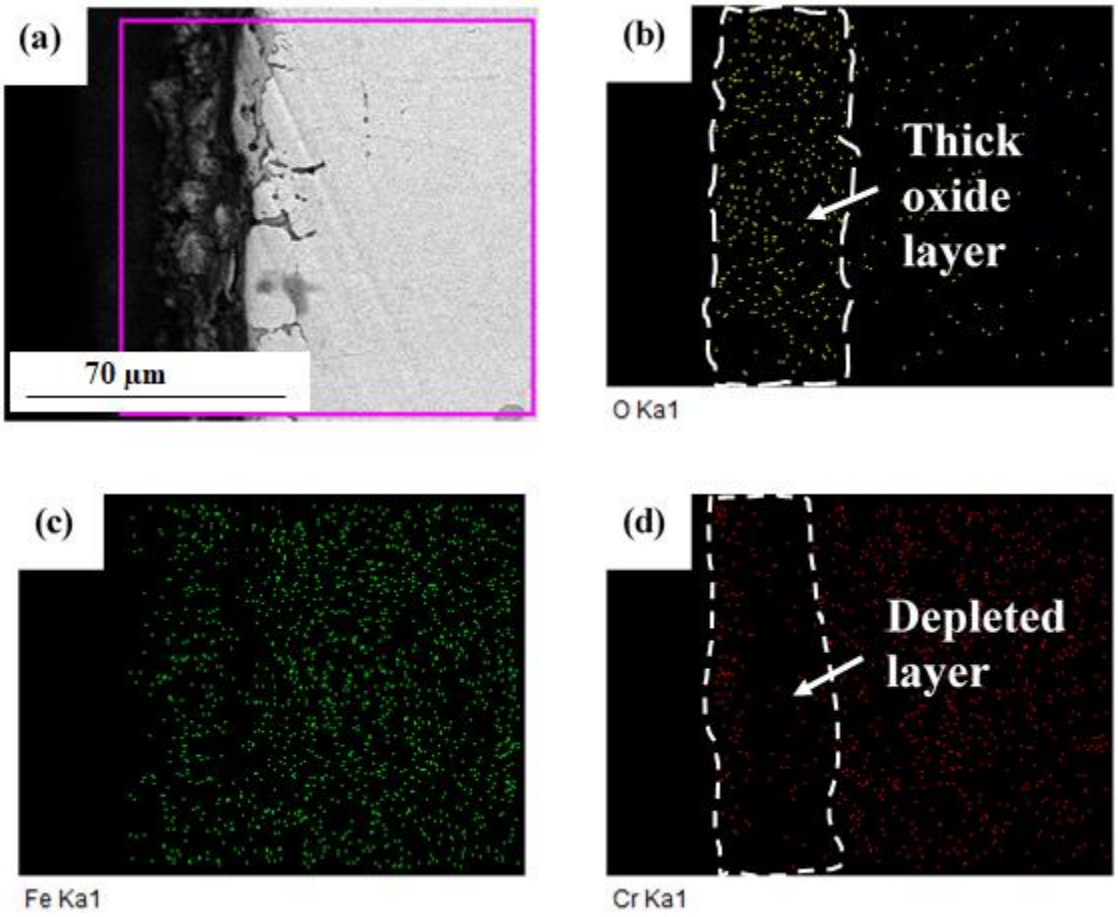

Fig. 7.13: Cross-sectional X-ray mapping of the salt mixture deposited 2min USSPed sample exposed at 750℃ for 20 h, focussing the elemental distribution **(a)** cross-section, **(b)** Oxygen, **(c)** Iron, and **(d)** Chromium.

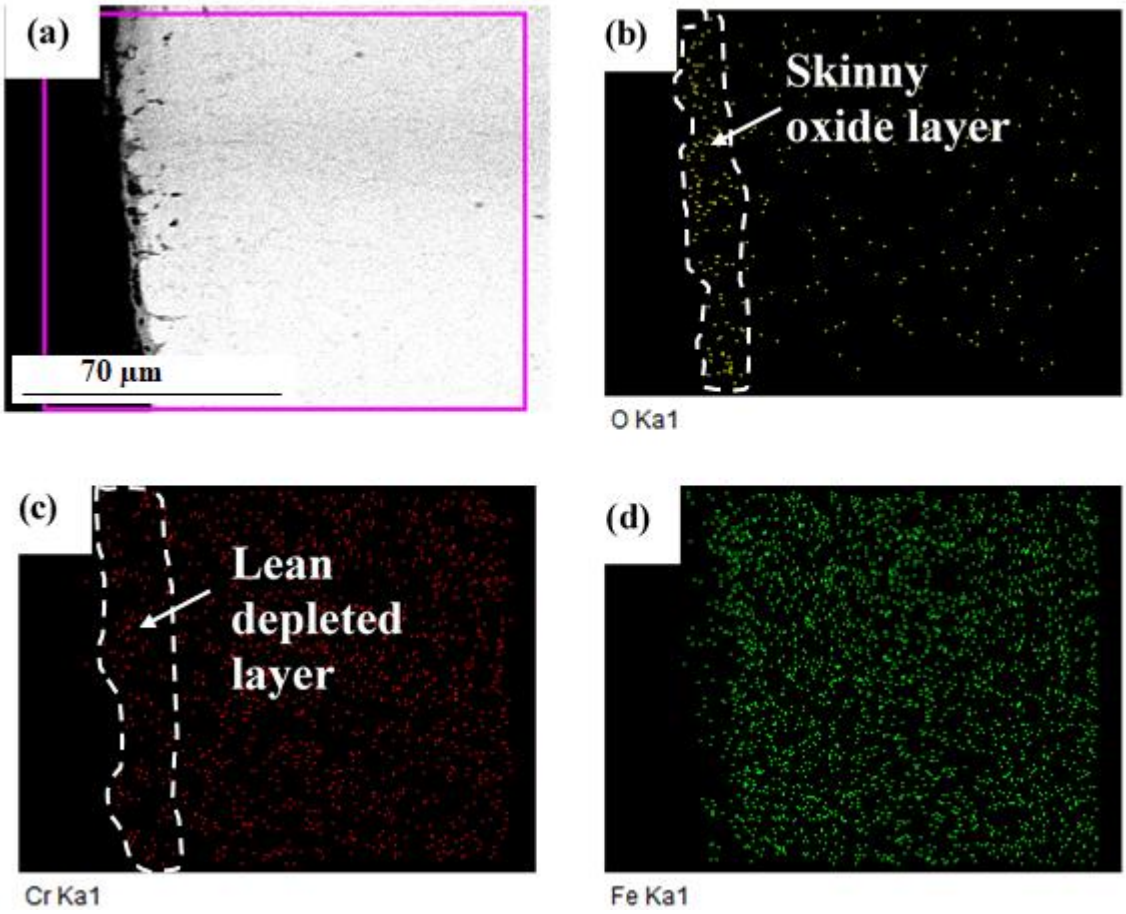

Fig. 7.14: Cross-sectional X-ray mapping of the salt mixture deposited 2min USSPed sample exposed at 750℃ for 20 h, focussing the elemental distribution **(a)** cross-section, **(b)** Oxygen, **(c)** Chromium, and **(d)** Iron.

7.2.3 High-temperature erosion wear of USSPed hot-corroded samples.

The wear scars formed under the variable impact of 30° and 90° at 550, 650 and 750℃ are shown in Fig. (7.15-7.17). At 550℃, the surface displays severe plastic deformation with large size indentations on the surface (Fig. 7.15). Erosion scars formed in the case of 650℃ (Fig. 7.16) show the mechanism of metal removal where the indentations are shallow. Along with this, ploughing and embedment of abrasives on the surface are also seen. Similar observations are made when scars from 750℃ samples are observed (Fig. 7.17). Clear impacts of erodent with larger plastic deformations, some

cracks, and plough marks are evident. Considering the effect of impact angle, at fixed temperature conditions, it is seen that more damage occurs at oblique impacts contrary to normal impacts, which proclaims the inverse relationship of impact angle with the erosion rate. The erosion curve has a static erosion rate concerning time (Fig. 7.18), which concludes that the erosion rate may not cause any dramatic influence on the physical appearance of the surface.

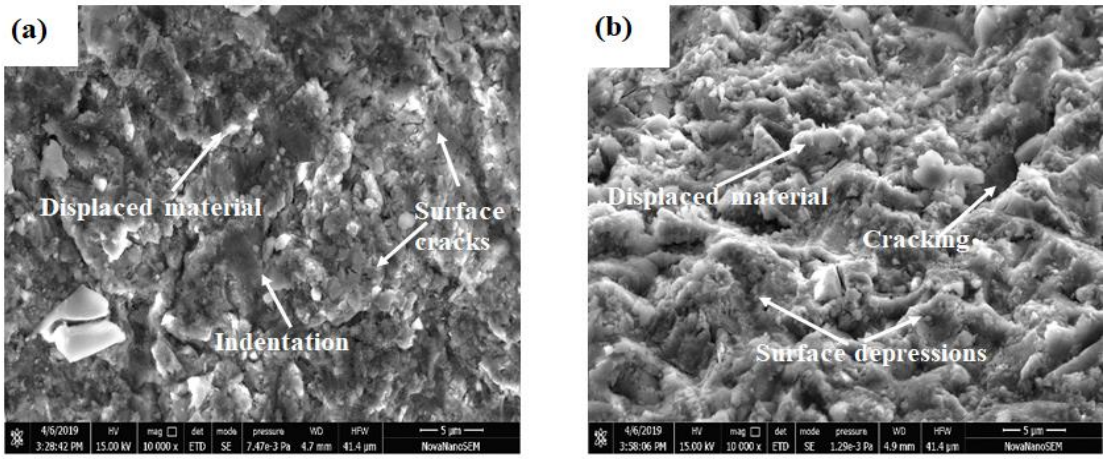

Fig. 7.15: SEM micrograph showing erosion scar at 550℃ for impingement angle of **(a)** 30°, and **(b)** 90°.

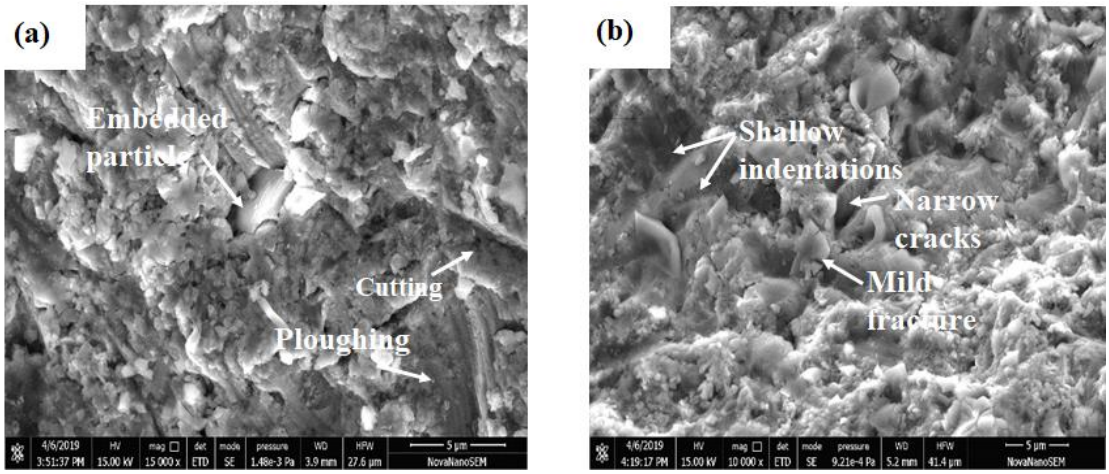

Fig. 7.16: SEM micrograph showing erosion scar at 650℃ for impingement angle of **(a)** 30°, and **(b)** 90°.

SEM micrographs shown in Figs. 7.15-7.17, represent entirely different mechanisms as compared to those observed in earlier studies [194]. In Fig.7.15a, the erosion at 550°C, and indentation and ploughing are evident at oblique impact. The plough marks are diminished, and the indentations take the shape of surface depressions when impacted at 90° angle (Fig. 7.15 b). At 650°C, the soft scale of ploughing is seen with some embedded particles on the surface (Fig.7.16a). Also, the surface depressions formed at normal impact are reduced (Fig. 7.16 b). At 750°C, no evidence of indentation is visible, rather, severe ploughing and cutting mechanism appears on the surface (Fig. 7.17 a). Some overturned material in the form of the removed layer due to cutting is visible in the erosion scars, which is responsible for higher material loss. At an intermediate angle of impact 60°, the erosion mechanism is seen to be similar to that under 30°. This statement can be substantiated with the erosion curve (Fig. 7.18) which is almost similar to the erosion rate at 30° angle.

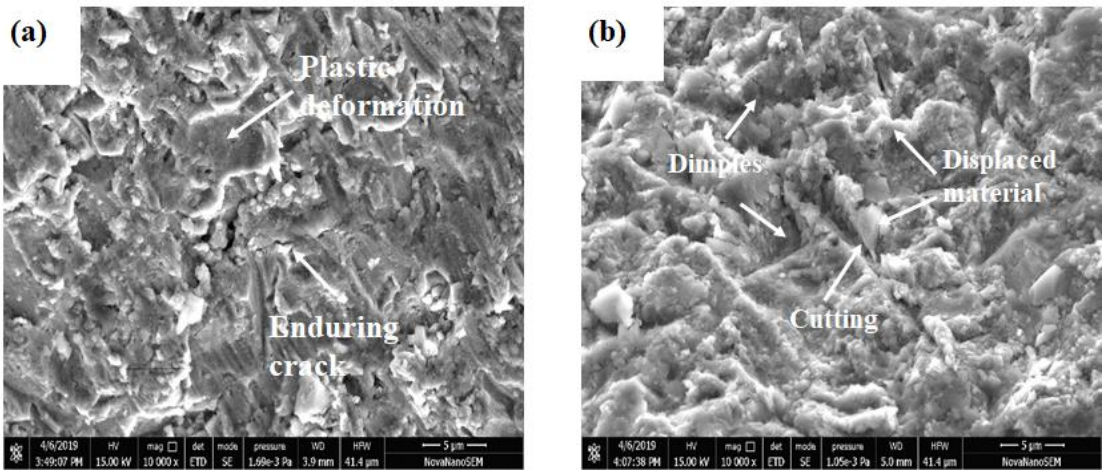

Fig. 7.17: SEM micrograph showing erosion scar at 750°C for impingement angle of **(a)** 30°, and **(b)** 90°.

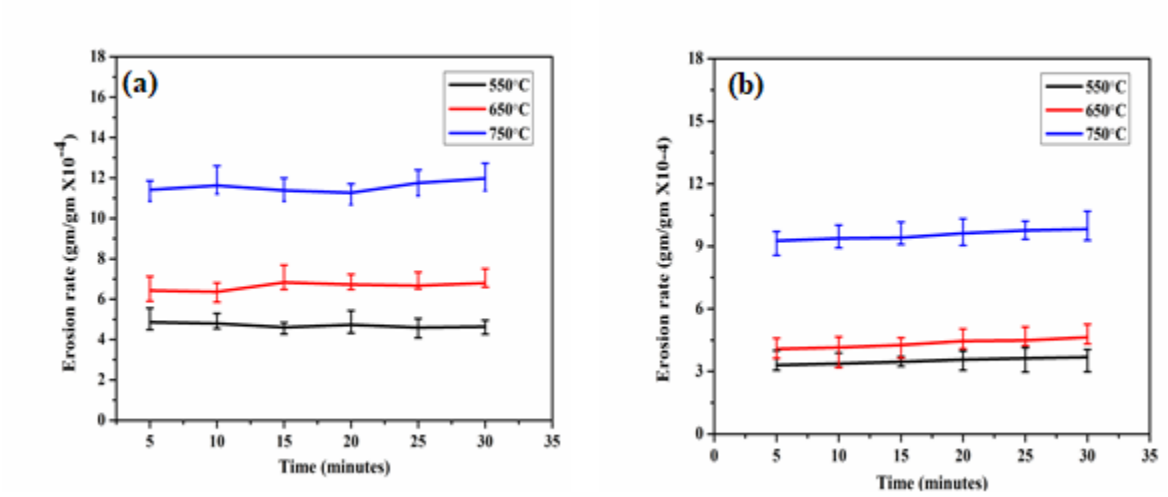

Fig.7.18: Erosion rate vs. impingement time at **(a)** 30° impingement angle, and **(b)** 90° impingement angle.

7.3 DISCUSSION

The effect of pre-hot corrosion-erosion has been investigated and presented in the last chapter [34]. This current study is determined to reduce material loss under the combined effect of hot corrosion-erosion. To fulfill the objective, surface modification through ultrasonic shot peening is carried out for variable duration. This technique develops SNC region on the surface to ~250 µm depth. Micro-hardness of the cross-sectioned surface varies from 342HV to 307HV and the formation of 65nm to 52nm grains (Fig. 7.6) binds to presume that the formation of nanograins occurred to a depth of 250 µm (Fig. 7.2). Also, the impact of steel balls generates plastic deformation and creates dimples over the surface in the form of peaks and valleys, and therefore, increases the surface roughness. The average surface roughness value has been observed to vary from 2.36 to 3.25µm for 1 min to 3 min of USSP duration respectively. With these clear findings, 3 min USSP showed relatively better surface properties, but the surface topography (Fig. 7.3 c) revealed that 3 min USSP suffers micro-chipping which renders the surface weak to resist

high impact erosion. Therefore, 2 min shot peening was chosen as an optimized condition for carrying out the study to mitigate the material loss.

It is obvious from the XRD profile that there is no phase transformation in Type 446SS under the impact of hardened steel balls which induces severe plastic deformation. And grain refinement resulting from USSP is reflected through peak broadening in magnified view (Fig. 7.5). The austenite transformed into strain reduced martensite is reported for 316L under USSP treatment [195]. The formation of nano-grains, which is evident in the bright-field TEM image is initiated by the formation of a slip system and their intersection resulting in the formation of extremely fine grains. The discontinuous ring in the SAD pattern signifies grain refinement (Fig. 7.7 d). Modification of surface using USSP led to large-scale grain refinement forming nanograins on the surface and thus the consistency of grain boundary increases. This increase in grain boundary is responsible for the diffusion of chromium and thereby forming a protective Cr_2O_3 layer. This thick formation of the Cr_2O_3 layer covers the grain boundaries and therefore, decreases the activity of oxygen on the treated surface resulting in enhancement of corrosion resistance [196]. It is observed that there is an insignificant weight change when exposed to 550℃ for 20 h. The XRD phase analysis and surface morphology of the sample at 550℃ clarifies the statement. However, significant weight gain is observed in the sample when exposed to 650 and 750℃ for the same duration. This aspect of surface deterioration is due to eutectic melting of the salt mixture being 628℃, where the available kinetics favours the salt to diffuse into the chromium oxide layer. The standard Gibbs Free Energies (ΔG_T) of product formation is listed in Table 7.2.

Table 7.2: ΔG_T of corrosion products formed at 650 and 750℃ [185].

Reactions forming corrosion products	ΔG_T (KJ/mol) [A + BT log T + CT]	
	at 750℃	at 650℃
$4Cr + 3O_2 \rightarrow 2Cr_2O_3$	-854.37	-880.31
$Cr_2O_3 + FeO \rightarrow FeCr_2O_4$	-447.03	-457.15
$Fe + Cl_2 \rightarrow FeCl_2$	-218.61	-229.91
$2Fe + \frac{3}{2}O_2 \rightarrow Fe_2O_3$	-105.73	-119.62

At temperature above 628℃, molten salt diffuses through capillary effect and forms slits and cracks on reacting with steel substrate. This causes oxidation and forms oxide scales initially. NaCl present in the salt mixture disintegrates into Na^+ and Cl^- ions. The Cl^- ions penetrate through the crack and form metal chlorides such as $CrCl_2$ and $FeCl_2$ on reacting with the substrate.

$$NaCl \rightarrow Na^+ + Cl^- \quad (7.3)$$

$$4FeCl_2 + 3O_2 \rightarrow 2Fe_2O_3 + 4Cl_2 \quad (7.4)$$

$$2Cr_2O_3 + 8Cl^- \rightarrow 4CrCl_2 + 3O_2 \quad (7.5)$$

$$Na_2O + Cr_2O_3 + \frac{1}{2}O_2 \rightarrow 2NaCrO_4 \quad (7.6)$$

$$4Fe + Na_2SO_4 \rightarrow 3FeO + FeS + Na_2O \quad (7.7)$$

The products formed on account of corrosion epitomized the increased concentration of iron and decreased the concentration of chromium, which illustrate the formation of the depleted zone beneath the oxide scale. Salt elements are seen to attack at the grain

boundaries and diffuse through the substrate forming fissure cracks, pits, slits, and narrow cracks. The rich content of oxygen shown on the surface in x-ray mapping is the strong evidence of the oxide scale formed. Chromium is considered as the most impactful element to counter hot-corrosion. This is due to its oxygen-pressure reliance for the basic dissolution of Cr_2O_3. The mechanism involving an electrochemical reduction of the solute of Cr in fused Na_2SO_4 has been discussed [197]. With an increase in time and temperature, the iron oxide layer seeks to grow thicker as long as the ionic salt present on the surface is totally consumed. This continuous growth of oxide induces stress, and once this stress level reaches the unbearable limit, these layers are removed in the form of flakes and lamina. The oxides previously formed reacts with $FeCl_2$ to form $FeCr_2O_4$ and Cl_2 gas. The Cl_2 gas causes fissure cracks and slits on evaporation, which emerge from the substrate and reach the surface. The density of crack and slits formed are dependent upon the reaction evolving Cl^- ions, and thus hot–corrosion is a temperature-dependent phenomenon. As temperature increases, the fluidity of molten salt increases which reacts with the oxide layer. The seeping of ionic salts increases the path size and the slits change into wide fissures cracks. Subsequently, rapid oxidation results due to the reaction between oxygen and iron forming iron-oxide and cause delamination of oxide layers.

High velocity impacting particles causes severe loss of the material by striking the surface and transforming their kinetic energy to cause deformation. X-ray diffraction shows no trace of corrosion products formed when exposed to 550°C and therefore, the erosion rate is in the same approximation as that of uncoated shot peened samples. With further increase in temperature, the products of corrosion formed are clearly seen in XRD and the presence of flakes is seen in the macrograph. Hence, an increase in the erosion

rate is witnessed. The process of material removal takes place from the corroded layer as well as from the SNC layer. A schematic presentation of the probable mechanism of erosion on SNC layer subjected to hot corrosion is shown in Fig. 7.19. The impact of steel balls develops dimples over the surface and forms a discrete layer of nanograins with peaks and valleys formed on the surface. The salt mixture deposition is thick in the valleys, and the peaks have thin layer deposition of the salt mixture which is due to their characteristic shape. The corroding species in the salt mixture penetrate in the bulk material through the valleys such that the salt mixture diffuses towards the interior and the alloying element diffuses towards the surface. This process of corrosion degrades the properties at the surface causing an increased rate of erosion and material loss [198]. The material removal is more pronounced at 750℃ as compared to 650℃ since the hot-corrosion products are more perilous. Therefore, the erosion rate increase is obvious at a higher temperature. Also, since no noticeable layer of oxide is observed, it is manifested that the growth rate of oxide formation may be excessively low.

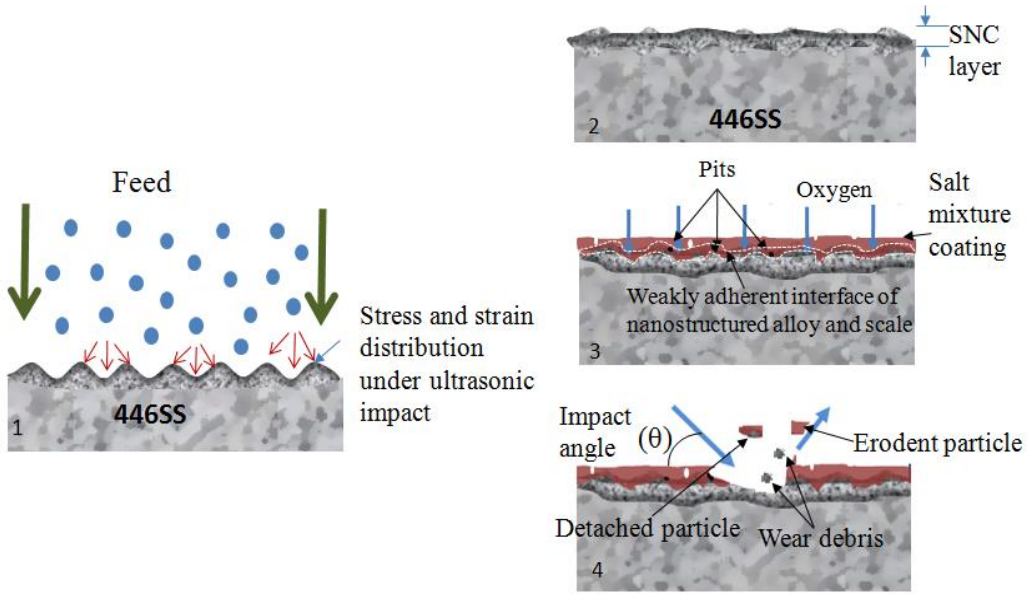

Fig.7.19: Schematic showing the effect of USSP on hot-corrosion on erosion of the Type 446SS at elevated temperature.

The large size indentations are responsible for material removal from the impact crater, but the detachment of material is meager, which is due to the SNC layer formed under the effect of shot-peening. Erosion scars formed (Fig. 7.16) show the mechanism of metal removal in the case of 650℃, where the indentations are shallow. Along with this, ploughing and embedment of abrasives on the surface are seen, which are responsible for greater loss of the material. Similar observations are made when scars from 750℃ samples are observed (Fig. 7.17). By clear impacts of erodent with larger plastic deformations, some cracks and plough marks are evident. Considering the effect of impact angle at fixed temperature conditions, it is seen that the shear force acting over the surface during impact curtails the response of the material to resist erosion under oblique impacts. Consequently, more damage is seen at oblique impacts as compared to normal impacts. The erosion curve (Fig. 7.18) in general, has a static erosion rate concerning time, but it varies proportionately concerning temperature. For a constant temperature, the impact angle shares an inverse relationship with the erosion rate. The oxide layer being indistinct and the incubation time is not noticeable, therefore, significant weight loss is seen in the first test cycle.

The eroded surface is discretized into three zones, discussed in Chapter 4.2 [176], where the central scar is most affected and becomes the sight for studying the mechanism taking place to cause erosion. The low angle metal cutting mechanism is taken over by large flake formation, deep indentations and minor cracks that have totally modified the appearance of the surface. These mechanisms are seen to operate in conjunction, and their contribution to the loss of material may vary depending upon the test temperature [181]. Indentation and ploughing at oblique impact with diminishing characteristics under 90° angle (Fig. 7.15 b), and the soft scale of ploughing with some embedded

particle on the surface (Fig. 7.16 a), are not the basic characteristics of this surface when impacted with high velocity and low impact angles. However, this behaviour may be attributed to the hard SNC layer formed on the material surface.

7.4 CONCLUSIONS

This study infers the following conclusions:

1. Ultrasonic shot peening caused grain refinement of nearly 65nm to a depth of 250 µm and led to the improvement of hot-corrosion resistance of Type 446SS at 550, 650 and 750℃.
2. USSP of Type 446SS led to high diffusivity of chromium on the surface from the alloy and formed a high corrosion resistance layer of Cr_2O_3 on the surface.
3. The relative increase in weight gain per unit area of pre-hot-corroded and ultrasonic shot-peened pre-hot corroded samples at 550, 650 and 750 were 55, 27.64 and 41.71% respectively.
4. The erosion rate is seen to vary proportionately with respect to temperature, and for any fixed temperature, the impact angle shares an inverse relationship with the erosion rate.
5. Large flake formation, deep indentations, and minor cracks are the mechanisms responsible for higher material loss. Also, in the wake of the hard SNC layer formed on the material surface, the soft scale of ploughing is seen with some embedded particles on the surface.